

Enhanced Photocatalytic Activity of Nanoparticle-Aggregated Ag–AgX(X = Cl, Br)@TiO₂ Microspheres Under Visible Light

Cuiling Zhang^{1,2} · Hao Hua² · Jianlin Liu² · Xiangyu Han² · Qipeng Liu² · Zidong Wei² · Chengbin Shao¹ · Chenguo Hu²

Received: 5 June 2017 / Accepted: 25 June 2017 / Published online: 19 July 2017
© The Author(s) 2017. This article is an open access publication

Highlights

- Ag–AgX(X = Cl, Br)@TiO₂ nanoparticle-aggregated spheres (NPAS) have been designed as a photocatalyst, in which AgX works as light harvester, Ag conducts as electron trapping and accumulating site, and TiO₂ acts as electron collecting and photocatalytic site.
- The photocatalytic activities of Ag–AgX(X = Cl, Br)@TiO₂ by degradation of methyl orange (MO) under visible light were improved by ~3 times relative to TiO₂ NPAS under simulated sunlight.

Abstract Ag–AgX(X = Cl, Br)@TiO₂ nanoparticle-aggregated spheres with different mass ratio of $R = \text{TiO}_2/\text{Ag}(X)$ from 35:1 to 5:1 were synthesized by a facile sol-gel technique with post-photoreduction. The photocatalytic activities of both Ag–AgCl@TiO₂ and Ag–AgBr@TiO₂ under visible light are effectively improved by ~3 times relative to TiO₂ NPAS under the simulated sunlight for the decomposition of methyl orange (MO). Ag–AgBr@TiO₂ showed 30% improvement and less stable in photocatalytic activity than that of AgCl@TiO₂. The role of Ag and AgX nanoparticles on the surface of Ag–AgX(X = Cl, Br)@TiO₂ was discussed. Ag on these samples not only

can efficiently harvest visible light especially for AgCl, but also efficiently separate excited electrons and holes via the fast electron transfer from AgX(X = Cl, Br) to metal Ag nanoparticles and then to TiO₂-aggregated spheres on the surface of heterostructure. On the basis of their efficient and stable photocatalytic activities under visible-light irradiation, these photocatalysts could be widely used for degradation of organic pollutants in aqueous solution.

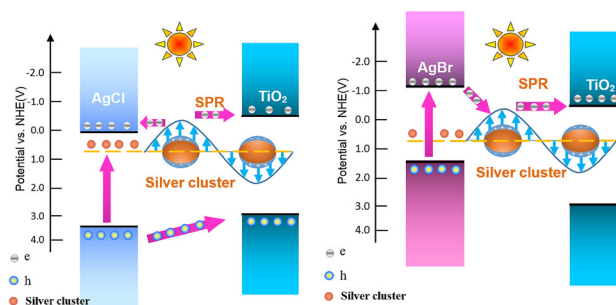
Electronic supplementary material The online version of this article (doi:10.1007/s40820-017-0150-8) contains supplementary material, which is available to authorized users.

✉ Cuiling Zhang
zhangcl@ctbu.edu.cn

✉ Chenguo Hu
hucg@cqu.edu.cn

¹ Chongqing Engineering Laboratory for Detection, Control and Integrated System, Chongqing Technology and Business University, Chongqing 400067, People's Republic of China

² College of Chemistry and Chemical Engineering, College of Physics, Chongqing University, Chongqing 400044, People's Republic of China



Keywords Ag–AgX(X = Cl, Br)@TiO₂ · Nanoparticle-aggregated spheres · Methyl orange · Visible light · Photocatalysis

1 Introduction

As an important photocatalyst, titanium dioxide (TiO_2) has been widely used in decomposition of toxic and hazardous organic pollutants, and in water splitting for hydrogen production [1–3]. However, the rapid recombination of photoinduced electrons and holes and its wide band gap greatly lower the TiO_2 quantum efficiency. Therefore, it is of great importance to improve the visible-light harvesting and the separation of photoinduced electron–hole pairs in TiO_2 for its further applications. TiO_2 -based heterostructures or composites formed by semiconductors with narrower band gap (e.g. $\text{Ag}_2\text{O}/\text{TiO}_2$, $\text{BiVO}_4/\text{TiO}_2/\text{BiVO}_4$, BiOI/TiO_2 , $\text{Cu}_2\text{O}/\text{TiO}_2$, and $\text{Bi}_2\text{O}_3/\text{TiO}_2$) have been intensively investigated to develop high activities [4–8]. In addition, noble metal– TiO_2 is used to improve the generation and separation of photoinduced carriers due to the surface plasmon resonance (SPR) of noble metal nanoparticles such as Ag and Pd [9–12]. The photoinduced electrons in noble metal transfer onto the surface of semiconductor, which results in visible-light photocatalytic activity, such as Ag/TiO_2 or Ag nanoparticles and graphene-co-loaded TiO_2 . Therefore, noble metal–semiconductor junction has potential application for the visible-light response in environmental purification. Specifically, because noble metal has a strong electron storage property and large work function, the excited electrons transfer from TiO_2 to a noble metal nanoparticle is an ultrafast process [9]. This phenomenon improves photocatalytic activity by effective charge separation. However, there are two opposite electron transfers in the metal–semiconductor structure which is from noble metal to semiconductor and from semiconductor to noble metal, respectively, under an irradiation. Thus, it is important to steer the transfer of the photoinduced carriers.

In recent years, AgX [13–22] and Ag/AgX ($X = \text{Cl}, \text{Br}$) have been paid much interest in the design of photosensitive composite materials because of their strong absorption of visible light by their surface plasmon resonance (SPR) and self-sensitization. It provides new opportunity for developing visible-light-driven photocatalyst. For example, it has been demonstrated that $\text{Ag}/\text{AgCl}-\text{BiOX}$ ($X = \text{Cl}, \text{Br}$) [16], $\text{Ag}/\text{AgCl}/\text{TiO}_2$ [17], and 3D $\text{AgX}/\text{graphene}$ aerogels ($X = \text{Br}, \text{Cl}$) [18], $\text{AgCl}_x\text{Br}_{1-x}$ nanocrystals [19], AgBr supported on $g\text{-C}_3\text{N}_4$ -decorated nitrogen-doped graphene ternary nanocomposites [20] and $\text{Ag}-\text{AgBr}/\text{TiO}_2$ composite [21] showed enhanced photocatalytic activities. In addition, the morphology of photocatalyst is important for the photocatalytic activity [23–28]. The pristine TiO_2 nanoparticles-aggregated spheres (NPAS), $\text{Ag}_2\text{O}/\text{TiO}_2$ NPAS, and Pt/TiO_2 NPAS showed excellent photocatalytic activity due to their large surface area and high adsorption of dyes [8, 24]. Meanwhile, because of its different band structures, AgX ($X = \text{Cl},$

Br) shows different photoresponsive behavior under visible light and the degradation mechanism of AgX ($X = \text{Cl}, \text{Br}$)/ TiO_2 on methyl orange (MO) might be different.

Herein, we developed a facile low-temperature method to prepare $\text{Ag}-\text{AgX}$ ($X = \text{Cl}, \text{Br}$)/ TiO_2 NPAS heterojunction photocatalysts and the influence of weight rate R ($R = \text{TiO}_2:\text{AgX}$) and band structures of heterojunctions on the photocatalytic activity were systematically studied. $\text{Ag}-\text{AgX}$ ($X = \text{Cl}, \text{Br}$)/ TiO_2 double heterostructures exhibited much higher photocatalytic activity for the degradation of MO under visible-light irradiation ($\lambda > 400 \text{ nm}$). The possible mechanism and the key role of metallic Ag on the photocatalytic activity of the $\text{Ag}-\text{AgX}$ ($X = \text{Cl}, \text{Br}$)/ TiO_2 double heterostructures were proposed.

2 Experimental Details

2.1 Preparation of Samples

All chemical reagents used in this experiment are of analytical purity and without further purification.

2.1.1 Preparation of $\text{Ag}-\text{AgCl}/\text{TiO}_2$ NPAS

TiO_2 NPAS were prepared by diglycol-mediated process with minor modification, which was reported elsewhere [24]. For $\text{Ag}-\text{AgCl}/\text{TiO}_2$ NPAS preparation, 0.23 g of TiO_2 NPAS was dispersed in 20 mL deionized water with vigorous stirring for 1 h, while 0.15 g cetyltrimethylammonium chloride (CTAC) was added dropwise to the suspension and stirred for 1 h. Then, 800 μL 0.1 mol L^{-1} AgNO_3 aqueous solution was added and continually stirred for 1 h and then irradiated for 30 min under the simulated sunlight. The precipitation was collected by a washing and centrifugation process, and then the obtained sample was dried at 60 °C in a drying oven for 12 h. Finally, the precursors were completely crystallized and converted into $\text{Ag}-\text{AgCl}/\text{TiO}_2$ NPAS by heating at 300 °C for 8 h in nitrogen. $\text{Ag}-\text{AgCl}/\text{TiO}_2$ with weight ratio ($R = \text{TiO}_2:\text{AgCl}$) of 1:0, 30:1, 25:1; 20:1; 15:1; 10:1; 5:1 denoted as sample S1–S7 was prepared by changing the amount of TiO_2 NPAS as shown in Table 1.

2.1.2 Preparation of $\text{Ag}-\text{AgBr}/\text{TiO}_2$ NPAS

The preparation of $\text{Ag}-\text{AgBr}/\text{TiO}_2$ NPAS is similar to that of $\text{Ag}-\text{AgCl}/\text{TiO}_2$, with cetyltrimethylammonium bromide (CTAB) added rather than CTAC. The $\text{Ag}-\text{AgCl}/\text{TiO}_2$ with weight ratio ($R = \text{TiO}_2:\text{AgBr}$) of 35:1, 30:1, 25:1, 20:1, 15:1, 10:1, 5:1 is denoted as sample S8–S14 as shown in Table 2.

Table 1 Experimental condition for the preparation of different Ag–AgCl@TiO₂ NPAS samples

Sample	TiO ₂ NPAS (g)	CTAC (g)	0.1 M AgNO ₃ aq. (μL)	R = TiO ₂ /AgCl
S2	0.3439	0.1536	800	30:1
S3	0.2866	0.1536	800	25:1
S4	0.2293	0.1536	800	20:1
S5	0.1719	0.1536	800	15:1
S6	0.1146	0.1536	800	10:1
S7	0.0573	0.1536	800	5:1

Table 2 Experimental condition for the preparation of different Ag–AgBr@TiO₂ NPAS samples

Sample	TiO ₂ NPAS (g)	CTAB (g)	0.1 M AgNO ₃ aq. (μL)	R = TiO ₂ /AgBr
S8	0.5257	0.1749	800	35:1
S9	0.4506	0.1749	800	30:1
S10	0.3755	0.1749	800	25:1
S11	0.3004	0.1749	800	20:1
S12	0.2253	0.1749	800	15:1
S13	0.1502	0.1749	800	10:1
S14	0.0751	0.1749	800	5:1

2.2 Characterization

X-ray photoelectron spectroscopy (XPS) patterns of Ag–AgX@TiO₂ NPAS were determined by photoelectron spectrometer (ESCALAB 250Xi). The morphological features of the samples were characterized by a scanning electron microscope (SEM, TESCAN VEGA 3 SBH SEM), a field emission scanning electron microscopy (FE-SEM, Nova 400 Nano SEM) and a high-resolution transmission electron microscopy (HRTEM, JEOL-4000EX). The elemental composition of the samples was recorded by energy-dispersive X-ray spectroscopy (EDS, OXFORD). UV–Vis absorption spectrum was measured by the UV–Vis spectrophotometer (UV-3600, Shimadzu) with an integrating sphere attachment. Photoluminescence (PL) measurement was obtained by an Edinburgh FLS920 fluorescence spectrometer with the excitation source of steady-state Xe900 450 W xenon lamp. All the measurement was taken at room temperature.

2.3 Photocatalytic Degradation

Twenty milligrams of samples was added into 50 mL aqueous suspension of MO (14 mg L⁻¹) in a 100 mL beaker. The suspension was magnetically stirred in dark for 30 min to establish adsorption/desorption equilibrium before illumination. An simulated sunlight instrument (CHF-XM-500 W) with a power of 100 mW cm⁻² was used as an illumination source, and the 420 nm cutoff filter was placed on the end of light transmission tube to ensure the irradiation only in visible-light wavelength. The catalysis after degradation was collected by a washing and

centrifugation process and then dried at 60 °C. In order to keep the mass of catalysis constant, some catalyst (about 2 mg) were added.

3 Results and Discussion

3.1 Crystal Structure, Morphology, and Formation Mechanism of Ag–AgX(X = Cl, Br)@TiO₂ NPAS

Figure 1a shows the XRD patterns of the Ag–AgCl@TiO₂ samples S1–S7. The sample S1 with R = 1:0 exhibits pure anatase phase TiO₂ (JCPDS No. 21-1272), while the rest of the sample S2–S7 show the diffraction peaks of pure cubic AgCl (JCPDS No. 31-1238) besides TiO₂. Both phases of AgCl and TiO₂ are consistent with that of the standard card. The XRD patterns of AgCl become strong from S2 to S7 with an increase of AgCl in AgCl@TiO₂. However, obvious Ag peaks are not found in the XRD patterns in all the samples. The 2-θ at 38.3° corresponding to the (111) of cubic phase Ag (Fm-3m (225), JCPDS No. 87-0719) appears to overlap with (004) (2-θ at 37.8°) and (112) (2-θ at 38.6°) of anatase phase TiO₂, and the small pimple of 2-θ at 77.7° may correspond to the (311) of cubic metallic Ag. Both of them do not demonstrably show the existence of Ag for XRD pattern, which demonstrates the Ag distributed on the AgCl@TiO₂ in a very small percentage. It is because there is a little elemental Ag reduced from AgCl under illumination for 30 min [29].

Figure 1b shows the XRD patterns of the Ag–AgBr@TiO₂ samples S8–S14. Similar to Ag–AgCl@TiO₂,

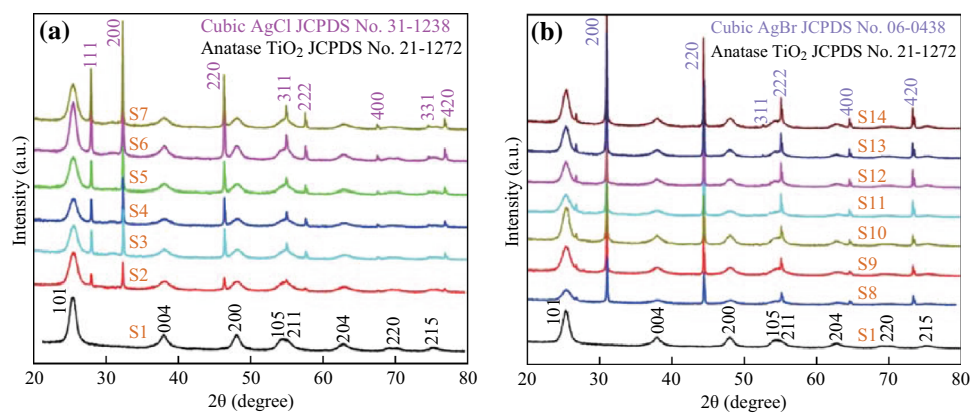


Fig. 1 XRD patterns of **a** the Ag-AgCl@TiO₂ NPAS samples and **b** Ag-AgBr@TiO₂ NPAS samples

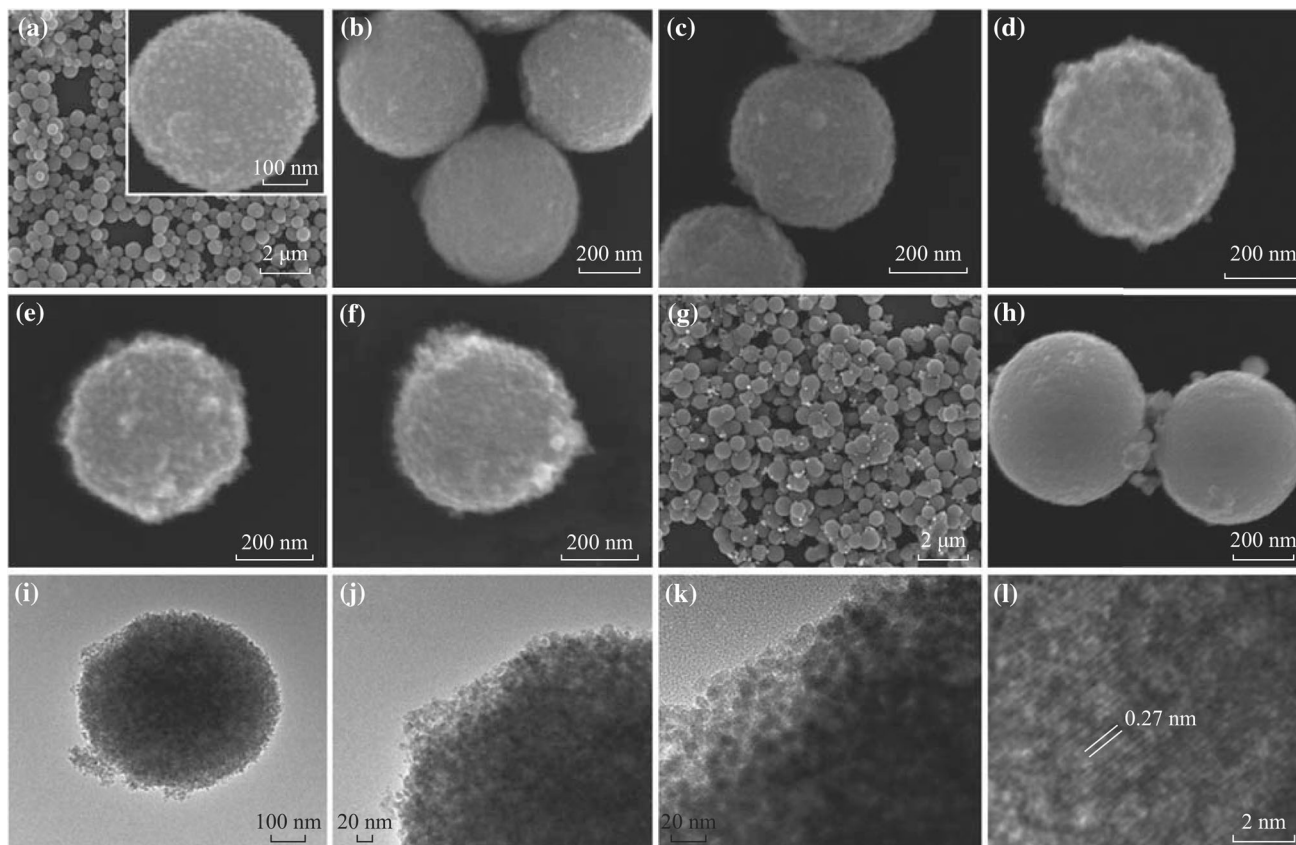


Fig. 2 FE-SEM images of Ag-AgCl@TiO₂ NPAS: **a** S1, **b** S2, **c** S3, **d** S4, **e** S5, **f** S6, **g-h** S7 and **i-l** TEM and HRTEM images of sample S4

the samples show two-phase mixture of cubic AgBr (*Fm*-3*m* (225), JCPDS No. 06-0438) and anatase phase TiO₂ and they are all consistent with those of the standard cards. The relative intensity of AgBr to TiO₂ increases with the decrease of R in Ag-AgBr@TiO₂. We do not have clear evidence of Ag existence from XRD and another measurement to confirm the Ag metal should be carried out.

To further obtain the structure and morphology information of Ag-AgX (X = Cl, Br)@TiO₂ samples, FE-SEM, TEM, and HRTEM characterizations have been conducted

as shown in Figs. 2 and 3. Figure 2a shows the FE-SEM and enlarged image in the inset of pristine TiO₂ (S1) which indicates nanoparticles-aggregated spheres with the diameter of 370–450 nm. The Ag-AgCl@TiO₂ with R from 30:1 to 5:1 (S1–S7) is shown in Fig. 2b–g, from which we can see that the diameter is about 500–600 nm with Ag-AgCl nanoparticles coated on the surface. The morphology of Ag-AgCl@TiO₂ is similar to that of the TiO₂-aggregated spheres, which indicates that the precipitation of Ag-AgCl on the surface of TiO₂ does not affect the structure of

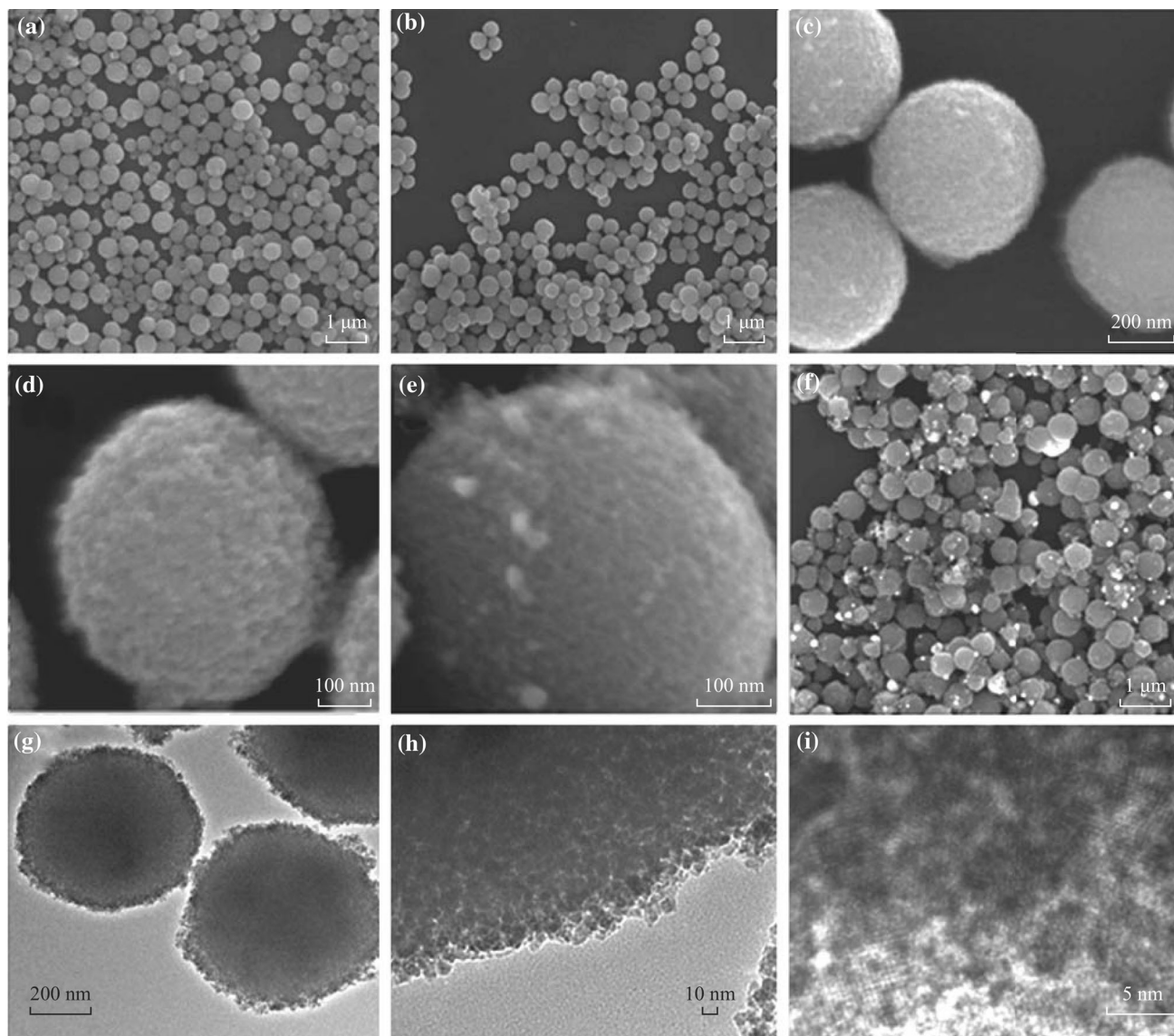


Fig. 3 FE-SEM images of Ag-AgBr@TiO₂ NPAS: **a** S8, **b** S9, **c** S10, **d** S12, **e** S13, **f** S14 and **g-i** TEM and HRTEM images of sample S11

TiO₂-aggregated spheres and TiO₂-aggregated spheres present very good sites to adsorb Ag-AgCl. With the increase of Ag-AgCl in Ag-AgCl@TiO₂, there are more and more small particles on the surface of samples. When R = 5:1, much larger particles of Ag-AgCl appear pinned on the spheres as shown in Fig. 2g and enlarged image in Fig. 2h. No individual particles of Ag-AgCl are found, which is similar to the Ag₂O-@TiO₂ NPAS [24]. The TEM and HRTEM of Ag-AgCl@TiO₂ with R = 20:1 named S4 are presented in Fig. 2i-l. The Ag-AgCl particles with a diameter of 5–15 nm are uniformly coated on the surface of the sample. These particles connect each other and the grain boundary can be seen. The perfect combination results from the lattice match of TiO₂ and AgCl. For example, the lattice spacing of (211) ($d = 0.167$ nm) and

(215) ($d = 0.126$ nm) for TiO₂ is close to that of (311) ($d = 0.167$ nm) and (331) ($d = 0.127$ nm) of AgCl provided by the XRD patterns in Fig. 1. The lattice fringe of AgCl is observed clearly in Fig. 2l, and the resolved interplanar distance is ca. 0.27 nm, corresponding to the (200) plane *e* of AgCl. The EDS analysis and elemental mapping images (EMIs) of O, Ti, Ag, and Cl of Ag-AgCl@TiO₂ are presented in Figs. S1b and S1c-f, respectively. The results reveal the uniform distributions of O, Ti, Ag, and Cl. Consequently, the Ag and AgCl nanoparticles are well distributed on the surface of TiO₂ nanoparticles-aggregated spheres.

Figure 3a-f shows FE-SEM images of Ag-AgBr@TiO₂ samples S8-S10 and S12-S14, respectively, from which we can see that Ag-AgBr nanoparticles are coated on the

surface of TiO_2 -aggregated spheres with the diameter of 500–600 nm. The morphology of Ag-AgBr@TiO_2 is similar to that of the TiO_2 -aggregated spheres, which indicates that the precipitation of Ag-AgBr on the surface of TiO_2 does not affect the structure of TiO_2 NPAS and TiO_2 NPAS present very good sites to adsorb Ag-AgBr . With the increase of Ag-AgBr in Ag-AgBr@TiO_2 , there are more and more small particles on the surface of samples. The TEM and HRTEM images of sample S11 are presented in Fig. 3g–i. The Ag-AgBr particles about 10 nm are uniformly coated on the surface of the samples and connect each other. The corresponding EDS analysis and EMIs of Ag-AgBr@TiO_2 are presented in Figs. S2b and S2c–f, which reveal the uniform distributions of O, Ti, Ag, and Br. Consequently, the Ag and Br are well distributed on the surface of TiO_2 nanoparticles-aggregated spheres.

The surface chemical states of the Ag-AgX ($X = \text{Cl, Br}$)@ TiO_2 with further investigation by XPS are shown in Fig. 4. The peak positions in all the XPS spectra were calibrated with C 1s at 286.4 eV. The XPS spectrum of the Ag-AgX ($X = \text{Cl, Br}$)@ TiO_2 indicates that the product

consists of Ag, Ti, O, and X ($X = \text{Cl, Br}$) elements (Fig. 4). The peak of N 1s results from the surface adsorption of nitrogen during preparation of Ag-AgX ($X = \text{Cl, Br}$)@ TiO_2 at 300 °C for 8 h under the protection of nitrogen. Two strong peaks at 464.3 and 458.6 eV are attributed to Ti 2p of TiO_2 (Fig. 4c), which is slightly shifted toward lower binding energies compared with that of pristine TiO_2 due to the direct contact between Ag nanoparticles and TiO_2 [21]. The peak of Cl can be divided into two peaks Cl 2p₃ and Cl 2p₁ peaks (Fig. 4d) [19], which correspond to 200.5 and 197.6 eV, respectively. Br 3d_{5/2} and Br 3d_{3/2} binding energies in XPS spectra correspond to 67.8 and 68.8 eV, respectively, which could be assigned to Br[−] in AgBr (Fig. 4e) [18]. There are two strong peaks for Ag 3d at about 374 and 367.8 eV as shown in Fig. 4f–g. The peaks at 374 and 367.8 eV can be divided into two peaks at about 374.2 and 373.4 eV, 367.4, and 368.4 eV, respectively. Two strong peaks at 373.4 and 367.4 eV are attributed to Ag 3d_{3/2} and Ag 3d_{5/2} of AgX in Ag-AgX ($X = \text{Cl, Br}$)@ TiO_2 . And the peaks at 374.2 and 368.4 eV are attributed to the metallic Ag of Ag 3d_{3/2} and Ag 3d_{5/2} in Ag-AgX ($X = \text{Cl, Br}$)@ TiO_2 .

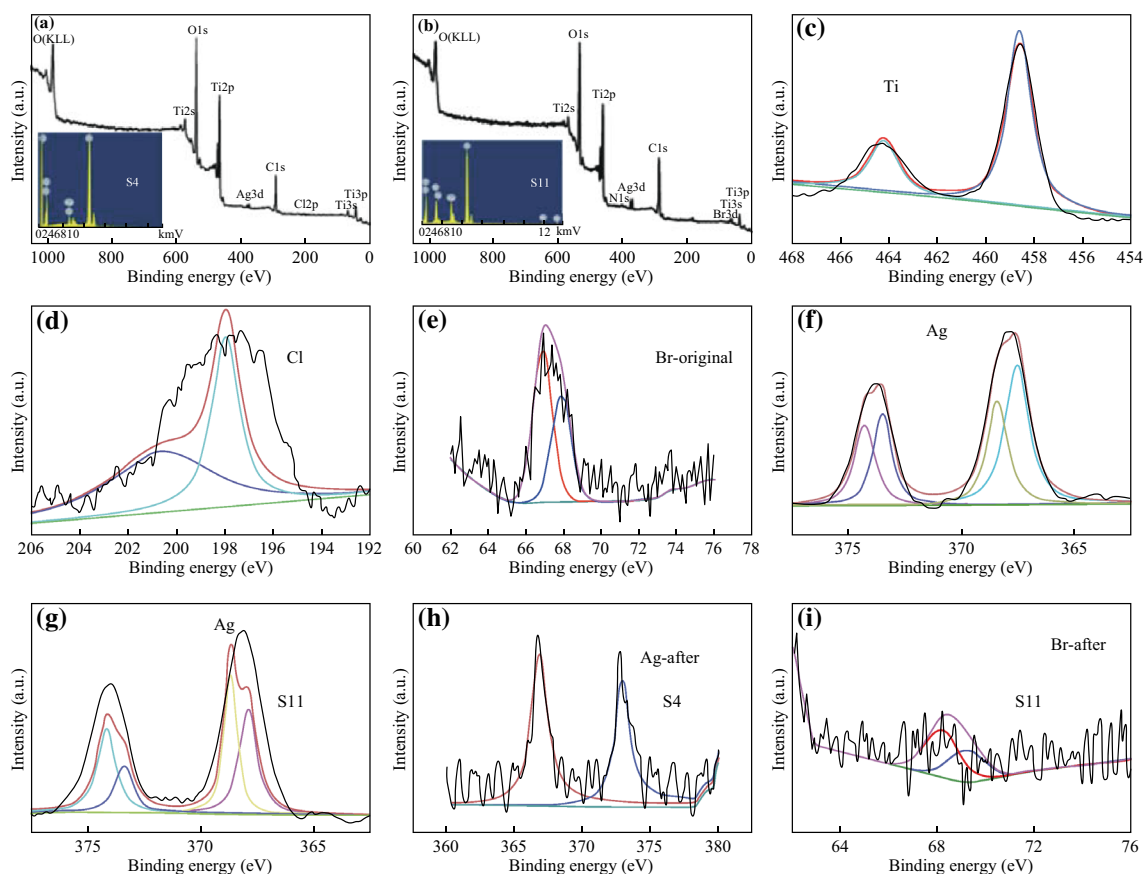


Fig. 4 XPS patterns of sample S4. Wide survey scan for **a** Ag-AgCl@TiO_2 and **b** Ag-AgBr@TiO_2 , **c** Ti 2p, **d** Cl 2p, **e** Br 3p, **f** Ag 3d and **g** Ag 3d of sample S11, **h** Ag 3d in S4 and **i** Br 3p in S11 after 5 cycles of photocatalytic degradation. The inset EDS patterns of samples 4 and 11 are in the inset in (a, b)

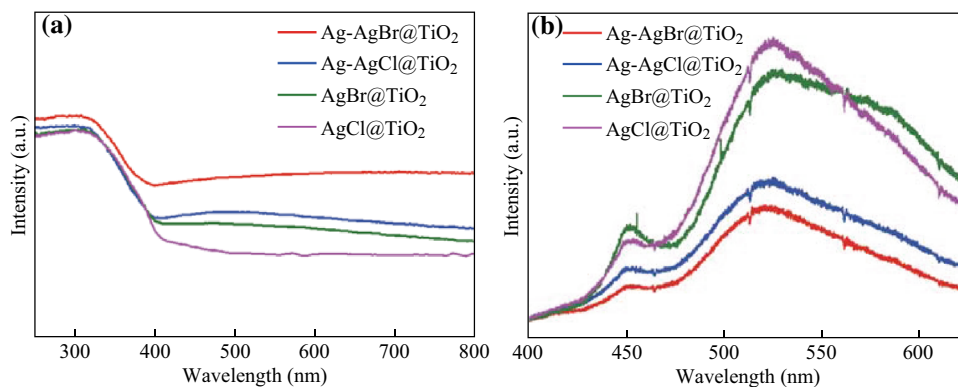
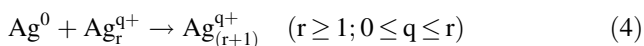


Fig. 5 **a** UV-Vis absorption spectra and **b** PL spectra of Ag-AgCl@TiO₂, Ag-AgBr@TiO₂, AgCl@TiO₂ and AgBr@TiO₂ structures

Br)@TiO₂ [17]. On the basis of XPS results, it can be confirmed that the coexistence of Ag(0) and AgX on the surface of TiO₂. EDS results are consistent with those of XPS, demonstrating distribution of Ag, Ti, O, and X (Cl, Br) on the samples as shown in the inset in Fig. 4a, b.

The element of Cl and Br comes from C₁₆H₃₃(CH₃)₃NCl (CTAC) and C₁₆H₃₃(CH₃)₃NBr (CTAB), respectively. Their long molecular chain, about 2.3–2.5 nm, is favorable to connect with TiO₂, but is not in tangle. On the basis of the above experimental results, a possible two-step growth mechanism for the formation of Ag-AgX(X = Cl, Br)@TiO₂ NPAS is proposed. In the first step, homogeneously distributed AgX(X = Cl, Br) nanoparticles on the surface of TiO₂-aggregated sphere are formed via an interaction between CTAC or CTAB and AgNO₃, which induces nanoparticles to assemble into the final AgX(X = Cl, Br)@TiO₂ microspheres. The microspheres of Ag-AgX(X = Cl, Br)@TiO₂ are formed in the second step when they are exposed to the simulated sunlight. Unbound metallic Ag (Ag⁰) appears due to the photo-induced reduction reaction of AgX nanoparticles. Free metallic Ag(Ag⁰) attaches each other on the surfaces of AgX(X = Cl, Br)@TiO₂ and forms the final Ag-AgX(X = Cl, Br)@TiO₂ NPAS. The reduced Ag⁰ atoms may also react with other silver species (Ag⁺ ions, Ag⁰ atoms, or silver clusters). The formation process is shown by the following equations [30]:



To understand the formation of Ag clusters and its role in photoactivity in Ag-AgX@TiO₂ NPAS, we prepared the AgX@TiO₂ NPAS in the same way without irradiation.

Figure 5a displays the UV-Vis absorption spectra of Ag-AgCl@TiO₂, Ag-AgBr@TiO₂, AgBr@TiO₂, and AgCl@TiO₂. It is well known that the band gap of anatase TiO₂ is about 3.2 eV. However, the absorption edge of the four samples is around 410 nm (about 3.1 eV), which is smaller than the band gap of anatase TiO₂. It might result from surface defect of nanoparticle aggregation spheres with large specific surface and imprecise measurement, which contribute to the absorption edge starting at a little larger wavelength [31]. In addition, AgCl and AgBr on the surface of TiO₂ have little influence on the absorption edge of Ag-AgX@TiO₂ NPAS. AgCl@TiO₂ has no absorption in visible light because of the large band gap of AgCl (about 3.3 eV), while AgBr@TiO₂ has weak absorption in the visible light due to its smaller band gap (about 2.6 eV). Obviously, Ag-AgCl@TiO₂ has weak visible-light absorption. Thus, the photoactivity of Ag-AgCl@TiO₂ extends from the UV into the visible-light region. The absorption of Ag-AgBr@TiO₂ in the range of 400–800 nm is stronger than that of AgBr@TiO₂ because of the emergence of Ag. Therefore, as the accumulated excited electrons on the surface of AgX combine with Ag⁺ to form Ag⁰ clusters under the simulated sunlight irradiation, Ag-AgX@TiO₂ is formed. Silver clusters have empty energy levels below the conduction band of AgCl, which enables a new electronic transition from the valence band of AgCl to the empty Ag cluster energy levels [30]. This is the well-known self-photosensitive property of AgX semiconductor, and it extends the light absorption from the UV to the visible region because of the silver clusters adsorbed on AgCl@TiO₂ surface [30]. The self-sensitization is different from the spectral sensitization effect of Ag clusters that makes an electron injection from Ag clusters into the AgCl conduction band [19]. Thus, the absorption in the visible light comes from the combined action of the surface plasmon resonance of metallic Ag and the self-sensitization effect of Ag clusters.

Silver clusters have contributed not only to light absorption but also the separation of the excited carriers.

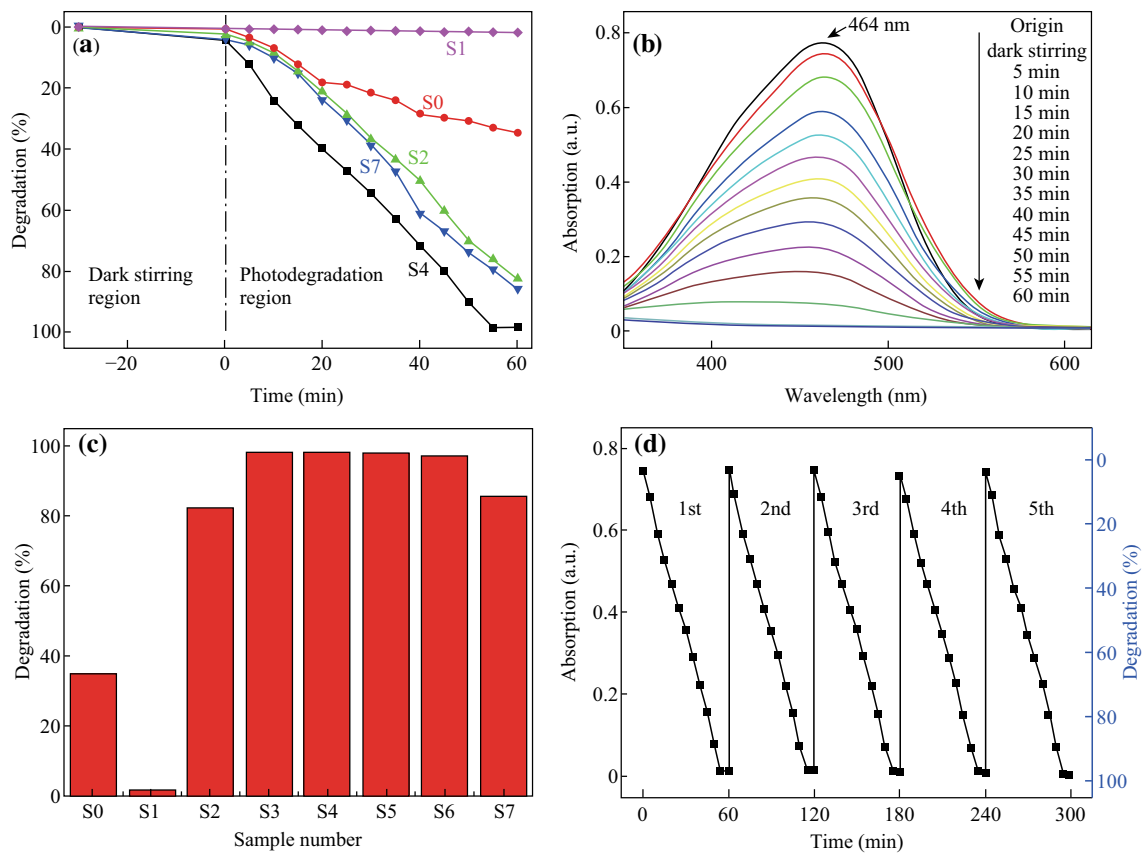


Fig. 6 **a** Comparisons of degradation rate with different samples in different stages; **b** absorption spectrums of the degradation with sample S4 in different stages; **c** comparisons of photocatalytic activities among the Ag–AgCl@TiO₂ NPAS samples with different *R* under the visible light irradiation and TiO₂ NPAS (S0) sample under the simulated sunlight irradiation in 60 min; **d** The result of the repeated experiments for five times with sample S4

The photoluminescence (PL) emission spectroscopy provides the separation efficiency of the electron–hole pairs and carrier lifetime in semiconductors [32]. The PL spectra of Ag–AgCl@TiO₂, Ag–AgBr@TiO₂, AgBr@TiO₂, and AgCl@TiO₂ (Fig. 5b) show two characteristic bands with peaks at 451 and 523 nm caused by the e–h recombination with 350 nm excitation, which correspond to the emission of TiO₂ [33]. The PL spectra are much similar for the four samples except for the strength. The PL intensity of Ag–AgX@TiO₂ shows a notable decrease compared with that of AgX@TiO₂. Thus, the decrease in the PL intensity suggests that Ag–AgX@TiO₂ NPAS possess a longer carrier lifetime, which demonstrates the enhancement of the photoinduced electron/hole pair separation. It is responsible for the enhanced photocatalytic activity for the pollutant degradation.

3.2 Visible-Light Photocatalytic Activity

MO is a kind of organic dye that is often used as a model pollutant to study the catalytic performance of photocatalysts. In this study, the photocatalytic activity of 20 mg

Ag–AgX (X = Cl, Br)@TiO₂ is assessed by observing the degradation of MO (14 mg L⁻¹) versus time under visible-light illumination (Figs. 6, 7). Before irradiation, the MO solution with the catalyst was kept in the dark for 30 min to reach the adsorption equilibrium. The concentration of the MO solution slightly decreases in the dark. Comparisons of photocatalytic activities among the Ag–AgCl@TiO₂ samples with different *R* under 60-min irradiation are shown in Fig. 6a, b. The degradation activity of sample S1 (TiO₂ NPAS) is hardly observed due to the larger band gap ($E_g = 3.2$ eV). But for the samples S2, S4, and S7, the corresponding degradation rates are 82%, 98%, and 85% under visible-light irradiation, which is much higher than that of S0 (TiO₂ NPAS under simulated sunlight, only 34.79%). It indicates that greatly improved photocatalytic activity is achieved by the heterostructure of Ag–AgCl@TiO₂, and the S4 with *R* = 20:1 exhibits highest activity for MO degradation as shown in Fig. 6a. The temporal evolution of the absorption spectra of MO aqueous solution in presence of S4 under visible-light irradiation is shown in Fig. 6b. The characteristic peaks centered at 464 nm do not change in position in degradation process.

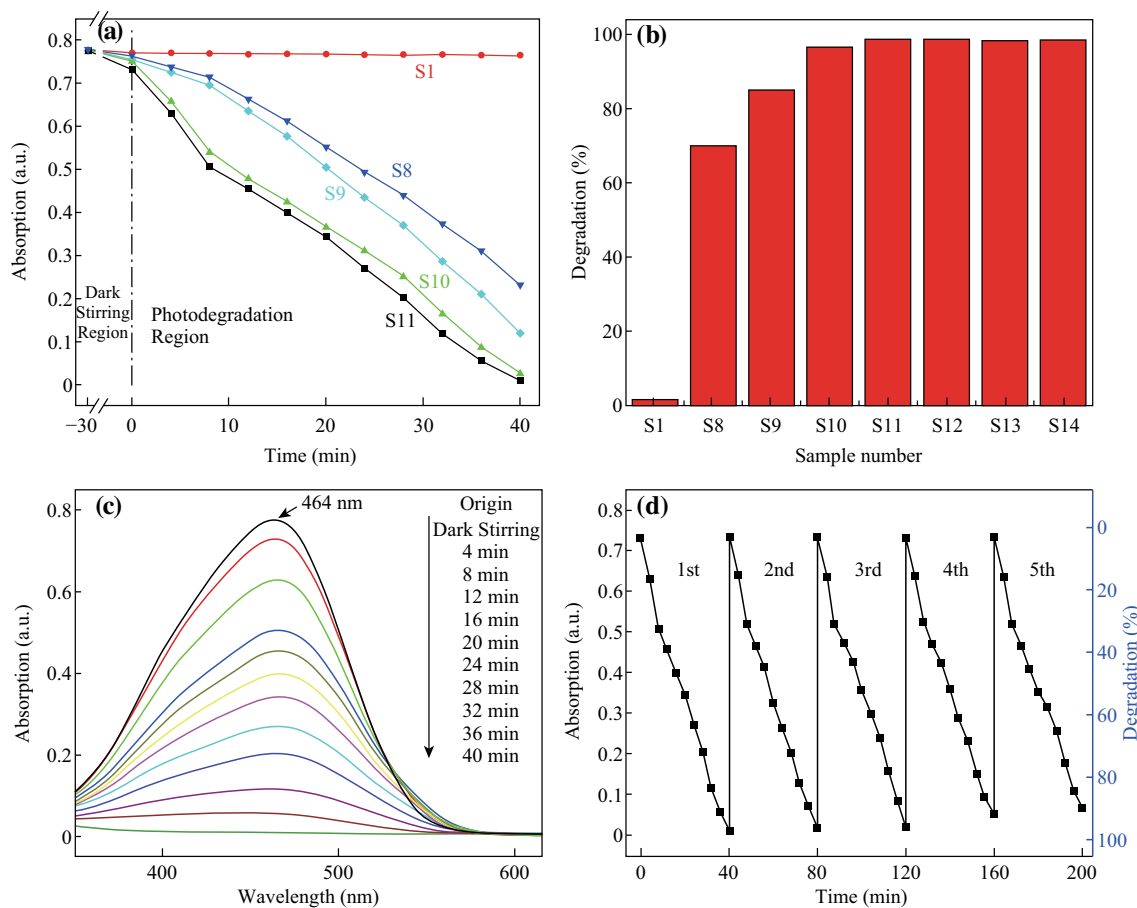


Fig. 7 **a** Comparisons of degradation rate with different samples in different stages; **b** comparisons of photocatalytic activities among the Ag-AgBr@TiO₂ NPAS samples with different R and TiO₂ NPAS sample under the visible light irradiation in 40 min; **c** absorption spectrums of the degradation with sample S11 in different stages; **d** the result of the repeated experiments for five times with sample S11

It indicates complete photocatalytic degradation of MO aqueous solution by the Ag-AgCl@TiO₂ NPAS during the reaction, and the catalyzed degradation intermediates are almost not produced. Histogram of photocatalytic activities of Ag-AgCl@TiO₂ NPAS with different R under visible-light irradiation for 60 min is shown in Fig. 6c. The samples with a wide range R from 10:1 to 25:1 exhibit higher activity for MO degradation with a degradation rate about 98%, which indicates a wide R range for application. It is important to be stable under repeated applications for an economical photocatalyst. Figure 6d shows the cycling performance of sample S4 for five cycles. The photocatalytic activity remains approximately 98%, revealing the excellent long-term photocatalytic stability of Ag-AgCl@TiO₂ NPAS.

Figure 7 exhibits the activity of Ag-AgBr@TiO₂ NPAS for MO degradation. It can be seen the efficient removal ratio of 98.78% (for sample S11) in 40 min, which is also far superior to those of Ag-AgCl@TiO₂ NPAS. Compared with Ag-AgCl@TiO₂ NPAS, Ag-AgBr@TiO₂ NPAS have an almost complete photocatalytic degradation of MO and

a wider R range from 25:1 to 5:1. Ever after five cycles, there is only about 7.25% of photocatalytic activity decrease for S11, indicating that Ag-AgBr@TiO₂ NPAS have excellent cycling photocatalytic activity.

3.3 Visible-Light Photocatalytic Mechanism of Ag-AgCl@TiO₂

To fully discuss the effects of the heterostructure on the photocatalytic activities of Ag-AgX (X = Cl, Br)@TiO₂ NPAS, the energy band diagram of Ag, AgX, and TiO₂ is presented in Fig. 8. AgCl has a direct band gap of 5.6 eV and an indirect band gap of 3.25 eV [21], and the band gap of AgBr is about 2.6 eV. Meanwhile, Ag-AgCl@TiO₂ NPAS can be excited by visible light as shown in Fig. 5a and it has self-photosensitive effect because of their point ionic defects and electron traps according to the Eqs. (1–5) [13, 34], which might help to photochemical decomposition. It is just similar to the research by Hu group that two electrons in one oxygen vacancy in CeO₂ are, respectively, excited to two Ce atoms neighboring the vacancy [35].

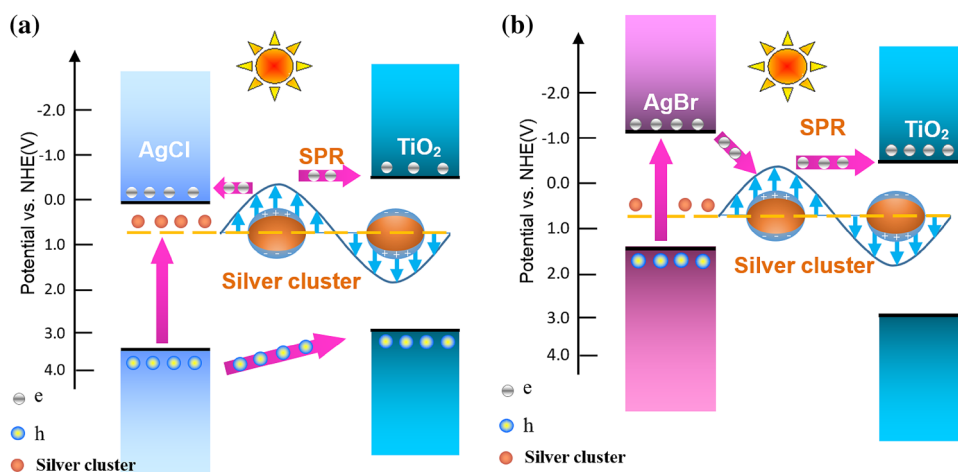


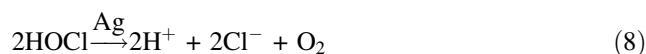
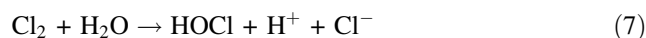
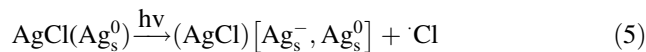
Fig. 8 Band structures and degradation mechanisms of **a** Ag–AgCl@TiO₂ NPAS and **b** Ag–AgBr@TiO₂ NPAS under visible light

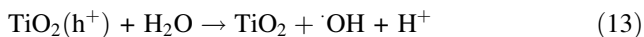
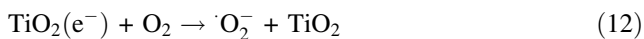
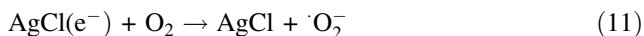
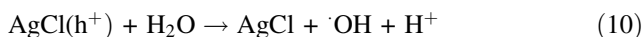
However, some researchers proposed that plasma resonance absorption of metallic Ag (or Pd) on the surface of semiconductor contributes to the effective visible absorption and segregation of electron/hole pairs, which results in the higher photocatalytic activity [9, 11, 12]. Liu et al. found that the double heterostructure Ag/TiO₂ nanoparticles/TiO₂ nanobelts have perfect photocatalytic properties under UV light irradiation with the dominant wavelength of 355 nm and Ag nanoparticles on the surface of the TiO₂ act as a sink for electrons contributing to the interfacial charge–transfer separation [36]. However, the composite photocatalyst with a wide weight ratio of TiO₂/Ag₂O exhibits a higher photocatalytic activity, but a bad cyclic stability under UV light irradiation because Ag⁺ is reduced to Ag [37]. Therefore, the role of Ag on the photocatalytic performance in Ag–AgCl@TiO₂ NPAS is not determined.

Thus, it is fascinating to consider how Ag/AgCl particles become an efficient and stable photocatalyst under visible light. To fully understand the photocatalysis process and the role of Ag nanoparticles during photocatalytic degradation MO, the XPS spectrum of the Ag–AgCl@TiO₂ after five cycles is presented in Fig. 4h. The two strong peaks at 373.4 and 367.4 eV corresponding to Ag3d_{3/2} and Ag 3d_{5/2} of AgCl in Ag/AgCl @TiO₂ become stronger, while the peaks at 374.2 and 368.4 eV corresponding to the metallic Ag of Ag 3d_{3/2} and Ag 3d_{5/2} become weaker. It indicates that some metallic Ag are oxidized to Ag⁺ and the self-sensitized effect of AgCl is suppressed during the photocatalysis reaction. Meanwhile, the XPS analysis and the photocatalysis under visible light prove that AgCl is stable at the photocatalytic degradation MO.

Therefore, the photocatalytic process of Ag–AgCl/TiO₂ under the visible light is as following. Firstly, under visible light irradiation, electrons on valence band of AgCl can be excited to empty silver cluster energy levels below the conduction band of AgCl and form photogenerated

electron–hole pairs due to the energy of light lower than the band gap of AgCl [30]. Subsequently, because the CB bottom (0.11 eV vs. NHE) and VB top (3.04 eV vs. NHE) of AgCl are below that of TiO₂ ($E_{CB} = -0.41$ eV, $E_{VB} = 2.37$ eV), respectively [17], most of excited electrons coming from the surface plasmonic resonance of Ag cluster transfer to the conduction band of AgCl and some excited electrons reach to the CB of TiO₂. The excited electrons react with O₂ adsorbed on the surface of the Ag–AgCl@TiO₂ NPAS to produce $\cdot\text{O}_2^-$ and H₂O₂ that successively decompose the MO to the final products. Holes transferring to the AgCl surface oxidize Cl[−] ions to $\cdot\text{Cl}$ radicals, which recombine very fast to form Cl₂, and then Cl₂ is reduced to chloride ions by reacting with H₂O under the applied conditions [13, 30]. Silver cations act as a catalyst for the decomposition of hypochlorous acid into molecular oxygen, protons, and chloride ions. Hypochlorous acid can also degrade the MO into micromolecule. Meanwhile, some holes also move to the valence band of TiO₂. The holes on the surface of TiO₂ can also oxidize OH[−] to yield $\cdot\text{OH}$. Therefore, the degradation of MO could be attributed to the reaction with $\cdot\text{O}_2^-$, $\cdot\text{OH}$, and H₂O₂ species during the photocatalysis. The excellent photocatalytic performance of Ag–AgCl@TiO₂ NPAS could be due largely to the improvement of electron/hole pairs separation after loading Ag–AgCl on the TiO₂. The reaction can be written as follows [17, 30],





Therefore, chlorine and hypochloric acid are inevitable during the photocatalytic reaction. Combining Eqs. (1) and (5–13), it indicates the excellent stability of Ag–AgCl@TiO₂ NPAS photocatalyst in the photocatalytic reaction under visible-light irradiation. Furthermore, it is well known that the Ag nanoparticles are likely to be slowly oxidized in the moist environment [13, 30]. Therefore, the XPS peaks of Ag⁺ become stronger after photocatalytic reaction.

In summary, as a promising candidate, Ag–AgCl@TiO₂ photocatalyst shows highly efficient and stable photocatalytic activities under visible light. Ag clusters play a significant role in the light harvesting, and the double heterostructure also plays a role in the prevention of the recombination of photogenerated electron–hole pairs.

3.4 Visible-Light Photocatalytic Mechanism of Ag–AgBr@TiO₂

Figure 8b shows the band structure of Ag, AgBr [16, 18, 19, 38], and TiO₂, which indicates the photocatalytic mechanism of the Ag–AgBr@TiO₂ photocatalyst. Under visible-light irradiation, electrons in AgBr ($E_{\text{CB}} = -0.67$ and $E_{\text{VB}} = 1.93$ eV) are excited from VB to CB for the narrow band gap of 2.6 eV and the photo-generated electrons easily transfer into metal Ag nanoparticles because the CB potential of AgBr is more negative than that Fermi level of the loaded metal Ag. Then some of the electrons in Ag from the AgBr transfer to the conduction band of TiO₂ ($E_{\text{CB}} = -0.41$ eV, $E_{\text{VB}} = 2.37$ eV) with the help of the Ag plasma resonance. The charge transfer process of AgBr → Ag → TiO₂ is similar to the efficient photosynthesis with charge flow steering [38–40]. The Ag clusters in the double heterojunction system act as a charge mediator for transferring electrons to the conduction band of TiO₂ and keeping holes in the valence band of AgBr. The stronger photoresponse in visible region and efficient carrier separation of Ag–AgBr@TiO₂ finally enhance the photocatalytic activity more than that of Ag–AgCl@TiO₂.

Since the XPS spectra of Br 3d_{5/2} and Br 3d_{3/2} in Ag–AgBr@TiO₂ photocatalyst become weak after five cycles of photocatalytic degradation MO as shown in Fig. 4i, AgBr in Ag–AgBr@TiO₂ NPAS is resolved into element Br and element Ag during the reaction of photocatalytic degradation MO according to the Eq. (2), which results in

the decrease of Ag–AgBr@TiO₂ NPAS on photocatalytic activity in degradation MO. However, the decomposition of AgBr does not obviously affect the photocatalytic activity, especially at the first three cycles because of the photocatalytic degradation of MO. Ag–AgBr@TiO₂ NPAS are excellent in a wider range ratio ($R = \text{TiO}_2/\text{AgBr}$) from 25:1 to 5:1, and then the stability of photocatalytic activity is gradually worse until R is larger than 25:1. The photocatalytic reaction of Ag–AgBr@TiO₂ agrees with the report of Yue group [38].

Owing to the self-sensitization, AgBr is easily decomposed into Ag and Br under visible-light irradiation. As a strong oxidant, Br photodegrades MO into CO₂ and H₂O. As a self-sacrificing of AgBr in Ag–AgBr@TiO₂ photocatalyst, the photodegradation of MO with Ag–AgBr@TiO₂ is similar to the Ag₂O/TiO₂ nanobelts reported by Liu et al. [25]. Therefore, the stability of Ag–AgBr@TiO₂ photocatalyst is slightly worse than that of Ag–AgCl@TiO₂.

4 Conclusions

In this paper, Ag–AgX (X = Cl, Br)@TiO₂ NPAS synthesized by a facile sol–gel technique and post-photoreduction method. On the basis of their efficient and stable photocatalytic activities, these photocatalysts could be widely used for environmental purification of organic pollutants in aqueous solution. As a self-sensitization material, both AgCl and AgBr have perfect photoresponse in visible light, especially AgBr. Both of them can efficiently separate excited electrons and holes via the fast electron transfer to metal Ag nanoparticles on the surface of heterostructure. The photocatalytic activity of Ag–AgBr@TiO₂ is higher than Ag–AgCl@TiO₂ at the first stage. This work indicates that, as an electronic transmission medium, metallic Ag can enhance photocatalytic activity not only via forming heterostructure with narrow band gap photocatalysts (e.g. $E_{\text{g}} = 2.6$ eV) but also for wide band gap photocatalysts (e.g. $E_{\text{g}} = 3.2$ eV) through the different roles. Ag nanoparticles on the surface of AgCl can effectively help to absorb visible light by self-sensitization and SPR and maintain stability of AgCl, while Ag nanoparticles in Ag–AgBr@TiO₂ system act as a charge mediator for transferring electrons from AgBr to TiO₂.

Acknowledgements This work is supported by the China Postdoctoral Science Foundation (2016M602647), the Science and Technology Research Project of Chongqing Municipal Education Commission of China (KJ1400607), the Fundamental Research Funds for the Central Universities (CQDXWL-2014-001), NSFCQ (cstc2015jcyjA20020), NSFC (51572040, 51402112), National High Technology Research and Development Program of China (2015AA034801).

Open Access This article is distributed under the terms of the Creative Commons Attribution 4.0 International License (<http://creativecommons.org/licenses/by/4.0/>), which permits unrestricted use, distribution, and reproduction in any medium, provided you give appropriate credit to the original author(s) and the source, provide a link to the Creative Commons license, and indicate if changes were made.

References

1. L. Wan, M. Long, D. Zhou, L. Zhang, W. Cai, Preparation and characterization of freestanding hierarchical porous TiO₂ monolith modified with graphene oxide. *Nano-Micro Lett.* **4**(2), 90–97 (2012). doi:[10.1007/BF03353698](https://doi.org/10.1007/BF03353698)
2. M. Boehme, W. Ensinger, Mixed phase anatase/rutile titanium dioxide nanotubes for enhanced photocatalytic degradation of methylene-blue. *Nano-Micro Lett.* **3**(4), 236–241 (2011). doi:[10.1007/BF03353678](https://doi.org/10.1007/BF03353678)
3. Y. Dong, J. Li, X. Li, B. Zhou, The promotion effect of low-molecular hydroxyl compounds on the nano-photoelectrocatalytic degradation of fulvic acid and mechanism. *Nano-Micro Lett* **8**(4), 320–327 (2016). doi:[10.1007/s40820-016-0091-7](https://doi.org/10.1007/s40820-016-0091-7)
4. M. Wang, W. Li, Y. Zhao, S. Gu, F.Z. Wang, H.D. Li, X.T. Liu, C.J. Ren, Synthesis of BiVO₄-TiO₂-BiVO₄ three-layer composite photocatalyst: effect of layered heterojunction structure on the enhancement of photocatalytic activity. *RSC Adv.* **7**(9), 75482–75490 (2016). doi:[10.1039/C6RA16796A](https://doi.org/10.1039/C6RA16796A)
5. J. Liu, L. Ruan, S.-B. Adeloju, Y. Wu, BiOI/TiO₂ nanotube arrays, a unique flake-tube structured p-n junction with remarkable visible-light photoelectrocatalytic performance and stability. *Dalton Trans.* **43**(4), 1706–1715 (2014). doi:[10.1039/C3DT52394B](https://doi.org/10.1039/C3DT52394B)
6. G.H. Jiang, R.J. Wang, Y. Wang, X.K. Sun, Preparation of Cu₂O/TiO₂ Composite porous carbon microspheres as efficient visible light-responsive photocatalysts. *Powder Technol.* **212**(1), 284–288 (2011). doi:[10.1016/j.powtec.2011.04.025](https://doi.org/10.1016/j.powtec.2011.04.025)
7. A. Rahman, Y.C. Ching, K.Y. Ching, A.K. Chakraborty, N.S. Liou, Surface modification of natural fiber using Bi₂O₃/TiO₂ composite for photocatalytic self-cleaning. *BioResources* **10**(4), 7405–7418 (2015). doi:[10.15376/biores.10.4.7405-7418](https://doi.org/10.15376/biores.10.4.7405-7418)
8. H. Hua, Y. Xi, Z.H. Zhao, X. Xie, C. Hu, H. Liu, Gram-scale wet chemical synthesis of Ag₂O/TiO₂ aggregated sphere heterostructure with high photocatalytic activity. *Mater. Lett.* **91**(2), 81–83 (2013). doi:[10.1016/j.matlet.2012.09.068](https://doi.org/10.1016/j.matlet.2012.09.068)
9. A. Takai, P.V. Kamat, Capture, store, and discharge shuttling photogenerated electrons across TiO₂-silver interface. *ACS Nano* **5**(9), 7369–7376 (2011). doi:[10.1021/nn202294b](https://doi.org/10.1021/nn202294b)
10. W.B. Li, F.X. Hua, J.G. Yue, J.W. Li, Ag@AgCl plasmon-induced sensitized ZnO particle for high-efficiency photocatalytic property under visible light. *Appl. Surf. Sci.* **285**(12), 490–497 (2013). doi:[10.1016/j.apsusc.2013.08.082](https://doi.org/10.1016/j.apsusc.2013.08.082)
11. F. Zhang, Z. Cheng, L. Cui, T. Duan, A. Anan, C. Zhang, L. Kang, Controllable synthesis of Ag@TiO₂ heterostructures with enhanced photocatalytic activities under UV and visible excitation. *RSC Adv.* **6**(3), 1844–1850 (2015). doi:[10.1039/C5RA17762F](https://doi.org/10.1039/C5RA17762F)
12. R. Long, K. Mao, M. Gong, S. Zhou, J. Hu et al., Tunable oxygen activation for catalytic organic oxidation: Schottky junction versus plasmonic effect. *Angew. Chem. Int. Ed.* **53**(12), 3205–3209 (2014). doi:[10.1002/anie.201309660](https://doi.org/10.1002/anie.201309660)
13. P. Wang, B. Huang, X. Qin, X.Y. Zhang, Y. Dai, J.Y. Wei, M.H. Whangbo, Ag@AgCl: a highly efficient and stable photocatalyst active under visible light. *Angew. Chem. Int. Ed.* **47**(41), 7931–7933 (2008). doi:[10.1002/anie.200802483](https://doi.org/10.1002/anie.200802483)
14. J. Yu, G. Dai, B. Huang, Fabrication and characterization of visible-light-driven plasmonic photocatalyst Ag/AgCl/TiO₂ nanotube arrays. *J. Phys. Chem. C* **113**(37), 16394–16401 (2009). doi:[10.1021/jp905247j](https://doi.org/10.1021/jp905247j)
15. J. Zhou, Y. Cheng, J. Yu, Preparation and characterization of visible-light-driven plasmonic photocatalyst Ag/AgCl/TiO₂ nanocomposite thin films. *J. Photochem. Photobiol., A* **223**(2), 82–87 (2011). doi:[10.1016/j.jphotochem.2011.07.016](https://doi.org/10.1016/j.jphotochem.2011.07.016)
16. L. Ye, J. Liu, C. Gong, L. Tian, T. Peng, L. Zan, Two different roles of metallic Ag on Ag/AgX/BiOX (X = Cl, Br) visible light photocatalysts: surface plasmon resonance and Z-scheme bridge. *ACS Catal.* **2**(8), 1677–1683 (2012). doi:[10.1021/cs300213m](https://doi.org/10.1021/cs300213m)
17. J. Cao, B. Xu, B. Luo, H. Lin, S. Chen, Preparation, characterization and visible-light photocatalytic activity of AgI/AgCl/TiO₂. *Appl. Surf. Sci.* **257**(16), 7083–7089 (2011). doi:[10.1016/j.apsusc.2011.03.046](https://doi.org/10.1016/j.apsusc.2011.03.046)
18. Y. Fan, W. Ma, D. Han, S. Gan, X. Dong, L. Niu, Convenient recycling of 3D AgX/graphene aerogels (X = Br, Cl) for efficient photocatalytic degradation of water pollutants. *Adv. Mater.* **27**(25), 3767–3773 (2015). doi:[10.1002/adma.201500391](https://doi.org/10.1002/adma.201500391)
19. B. Cai, J. Wang, D. Han, S. Gan, Q. Zhang, Z. Wu, L. Niu, Ternary alloyed AgCl_xBr_{1-x} nanocrystals: facile modulation of electronic structures toward advanced photocatalytic performance. *Nanoscale* **5**(22), 10989–10995 (2013). doi:[10.1039/c3nr03365a](https://doi.org/10.1039/c3nr03365a)
20. H. Li, S. Gan, H. Wang, D. Han, L. Niu, Intercorrelated super-hybrid of AgBr supported on graphitic C₃N₄-decorated nitrogen-doped graphene: high engineering photocatalytic activities for water purification and CO₂ reduction. *Adv. Mater.* **27**(43), 6906–6913 (2015). doi:[10.1002/adma.201502755](https://doi.org/10.1002/adma.201502755)
21. X. Wang, Y. Tang, Z. Chen, T.T. Lim, Highly stable heterostructured Ag-AgBr/TiO₂ composite: a bifunctional visible-light active photocatalyst for destruction of ibuprofen and bacteria. *J. Mater. Chem.* **22**(43), 23149–23158 (2012). doi:[10.1039/c2jm35503e](https://doi.org/10.1039/c2jm35503e)
22. J. Tejada, N.J. Shevchick, W. Braun, A. Goldmann, M. Cardona, Valence bands of AgCl and AgBr: UV photoemission and theory. *Phys. Rev. B* **12**(12), 1557–1566 (1975). doi:[10.1103/PhysRevB.12.1557](https://doi.org/10.1103/PhysRevB.12.1557)
23. S. Higashimoto, Y. Nakai, M. Azuma, M. Takahashi, Y. Sakata, One-pot synthesis of imine from benzyl alcohol and nitrobenzene on visible-light responsive CdS-TiO₂ photocatalysts. *RSC Adv.* **4**(71), 37662–37668 (2014). doi:[10.1039/C4RA06231K](https://doi.org/10.1039/C4RA06231K)
24. H. Hua, C.G. Hu, Z.H. Zhao, H. Liu, X. Xie, Y. Xi, Pt nanoparticles supported on submicrometer-sized TiO₂ spheres for effective methanol and ethanol oxidation. *Electrochim. Acta* **105**(26), 130–136 (2013). doi:[10.1016/j.electacta.2013.05.002](https://doi.org/10.1016/j.electacta.2013.05.002)
25. G. Prieto, H. Tüysüz, N. Duyckaerts, J. Knossalla, G. Wang, F. Schüth, Hollow nano- and microstructures as catalysts. *Chem. Rev.* **116**(22), 14056–14119 (2016). doi:[10.1021/acs.chemrev.6b00374](https://doi.org/10.1021/acs.chemrev.6b00374)
26. Q. Li, F. Wang, L. Sun, Z. Jiang, T. Ye, M. Chen, Q. Bai, C. Wang, X. Han, Design and synthesis of Cu@CuS yolk-shell structures with enhanced photocatalytic activity. *Nano-Micro Lett.* **9**(3), 35 (2017). doi:[10.1007/s40820-017-0135-7](https://doi.org/10.1007/s40820-017-0135-7)
27. H. Wei, L. Wang, Z. Li, S. Ni, Q. Zhao, Synthesis and photocatalytic activity of one-dimensional CdS@TiO₂ core-shell heterostructures. *Nano-Micro Lett.* **3**(1), 6–11 (2011). doi:[10.1007/BF03353645](https://doi.org/10.1007/BF03353645)
28. P. Zhang, L. Wang, X. Zhang, J. Hu, G. Shao, Three-dimensional porous networks of ultra-long electrospun SnO₂ nanotubes with high photocatalytic performance. *Nano-Micro Lett.* **7**(1), 86–95 (2015). doi:[10.1007/s40820-014-0022-4](https://doi.org/10.1007/s40820-014-0022-4)

29. W. Liu, D. Chen, S.H. Yoo, S.O. Cho, Hierarchical visible-light-response Ag/AgCl@TiO₂ plasmonic photocatalysts for organic dye degradation. *Nanotechnology* **24**(40), 405706 (2013). doi:[10.1088/0957-4484/24/40/405706](https://doi.org/10.1088/0957-4484/24/40/405706)
30. G. Calzaferri, D. Brühwiler, S. Glaus, D. Schürch, A.o Currao, C. Leiggener, Quantum-sized silver, silver chloride and silver sulfide clusters. *J. Imaging Sci. Technol.* **45**(4), 331–339 (2001)
31. W.J. Zhou, L.G. Gai, P.G. Hu, J.J. Cui, X.Y. Liu et al., Phase transformation of TiO₂ nanobelts and TiO₂ (B)/anatase interface heterostructure nanobelts with enhanced photocatalytic activity. *CrystEngComm* **13**(22), 6643–6649 (2011). doi:[10.1039/c1ce05638g](https://doi.org/10.1039/c1ce05638g)
32. H.F. Dang, X.F. Dong, Y.C. Dong, Y. Zhang, S. Hampshire, TiO₂ nanotubes coupled with nano-Cu(OH)₂ for highly efficient photocatalytic hydrogen production. *Int. J. Hydrog Energy* **38**(5), 2126–2135 (2013). doi:[10.1016/j.ijhydene.2012.11.135](https://doi.org/10.1016/j.ijhydene.2012.11.135)
33. Y. Sang, Z. Zhao, J. Tian, P. Hao, H. Jiang, H. Liu, J.P. Claverie, Enhanced photocatalytic property of reduced graphene oxide/TiO₂ nanobelt surface heterostructures constructed by an in situ photochemical reduction method. *Small* **10**(18), 3775–3782 (2014). doi:[10.1002/smll.201303489](https://doi.org/10.1002/smll.201303489)
34. J.F. Hamilton, Physical properties of silver halide microcrystals. *Photogr. Sci. Eng.* **18**(5), 493–500 (1974)
35. Y. Kang, Q. Leng, D.L. Guo, D.Z. Yang, Y.P. Pu, C.G. Hu, Room-temperature magnetism of ceria nanocubes by inductively transferring electrons to Ce atoms from nearby oxygen vacancy. *Nano-Micro Lett.* **8**(1), 13–19 (2016). doi:[10.1007/s40820-015-0056-2](https://doi.org/10.1007/s40820-015-0056-2)
36. W.J. Zhou, G.J. Du, P.G. Hu, G.H. Li, D.Z. Wang et al., Nanoheterostructures on TiO₂ nanobelts achieved by acid hydrothermal method with enhanced photocatalytic and gas sensitive performance. *J. Mater. Chem.* **21**(22), 7937–7945 (2011). doi:[10.1039/c1jm10588d](https://doi.org/10.1039/c1jm10588d)
37. W. Zhou, H. Liu, J. Wang, D. Liu, G. Du, J. Cui, Ag₂O/TiO₂ nanobelts heterostructure with enhanced ultraviolet and visible photocatalytic activity. *ACS Appl. Mater. Interfaces.* **2**(8), 2385–2392 (2010). doi:[10.1021/am100394x](https://doi.org/10.1021/am100394x)
38. X. Liu, D. Zhang, B. Guo, Y. Qu, G. Tian, H. Yue, S. Feng, Recyclable and visible light sensitive Ag–AgBr/TiO₂: surface adsorption and photodegradation of MO. *Appl. Surf. Sci.* **353**, 913–923 (2015). doi:[10.1016/j.apsusc.2015.06.206](https://doi.org/10.1016/j.apsusc.2015.06.206)
39. S. Liu, C. Han, Z.R. Tang, Y.J. Xu, Heterostructured semiconductor nanowire arrays for artificial photosynthesis. *Mater. Horiz.* **3**(4), 270–282 (2016). doi:[10.1039/C6MH00063K](https://doi.org/10.1039/C6MH00063K)
40. J.L. Liu, C.L. Zhang, B. Ma, T. Yang, X. Gu, X. Wang, C.G. Hu, Rational design of photoelectron-trapped/accumulated site and transportation path for superior photocatalyst. *Nano Energy* **38**, 271–280 (2017). doi:[10.1016/j.nanoen.2017.05.052](https://doi.org/10.1016/j.nanoen.2017.05.052)